Journal of Biomechanics 46 (2013) 165–169

Contents lists available at SciVerse ScienceDirect

Journal of Biomechanics

journal homepage: www.elsevier.com/locate/jbiomech
www.JBiomech.com

Short communication

Serial analysis of lumen geometry and hemodynamics in human arteriovenous fistula for hemodialysis using magnetic resonance imaging and computational fluid dynamics

Yong He [a,b,1], Christi M. Terry [c,1], Cuong Nguyen [c], Scott A. Berceli [a,b], Yan-Ting E. Shiu [c,d,*], Alfred K. Cheung [c,e,*]

[a] Department of Surgery, University of Florida, Gainesville, FL, USA
[b] Malcom Randall Veterans Affairs Medical Center, Gainesville, FL, USA
[c] Division of Nephrology and Hypertension, University of Utah School of Medicine, Salt Lake City, UT, United States
[d] Department of Bioengineering, University of Utah, Salt Lake City, UT, USA
[e] Medical Care Center, Veterans Affairs Salt Lake City Healthcare System, Salt Lake City, UT, USA

ARTICLE INFO

Article history:
Accepted 3 September 2012

Keywords:
Hemodialysis
Arteriovenous fistula
Wall shear stress
Computational fluid dynamics
Magnetic resonance imaging

ABSTRACT

The arteriovenous fistula (AVF) is the preferred form of vascular access for maintenance hemodialysis, but it often fails to mature to become clinically usable, likely due to aberrant hemodynamic forces. A robust pipeline for serial assessment of hemodynamic parameters and subsequent lumen cross-sectional area changes has been developed and applied to a data set from contrast-free MRI of a dialysis patient's AVF collected over a period of months after AVF creation surgery. Black-blood MRI yielded images of AVF lumen geometry, while cine phase-contrast MRI provided volumetric flow rates at the in-flow and out-flow locations. Lumen geometry and flow rates were used as inputs for computational fluid dynamics (CFD) modeling to provide serial wall shear stress (WSS), WSS gradient, and oscillatory shear index (OSI) profiles. The serial AVF lumen geometries were co-registered at 1 mm intervals using respective lumen centerlines, with the anastomosis as an anatomical landmark. Lumen enlargement was limited at the vein region near the anastomosis and a downstream vein valve, potentially attributed to the physical inhibition of wall expansion at those sites. This work is the first serial and detail study of lumen and hemodynamic changes in human AVF using MRI and CFD. This novel protocol will be used for a multicenter prospective study to identify critical hemodynamic factors that contribute to AVF maturation failure.

© 2012 Elsevier Ltd. All rights reserved.

1. Introduction

The arteriovenous fistula (AVF) is the preferred vascular access for chronic hemodialysis due to lower rates of infection and stenosis than other access types once the AVFs become matured. AVF maturation is characterized by marked luminal dilatation with increased blood flow in the venous portion following its surgical creation. Unfortunately, up to 60% of AVFs never adequately mature (Dember et al., 2008; Biuckians et al., 2008). Typically the lumen fails to enlarge or is reduced by neointimal hyperplasia.

Hemodynamic wall shear stress (WSS) is likely important to the AVF maturation process. Computational fluid dynamics (CFD) analysis of WSS in AVFs has been performed using data obtained from angiography (Ene-Iordache et al., 2001) or MRI (Niemann et al., 2012). However, there has been no published in-depth serial study in human AVF that is essential for understanding the role of WSS in AVF maturation. A multicenter prospective study is currently underway to identify critical hemodynamic factors contributing to AVF maturation or failure. We report here as a proof of concept, the development and application of a robust MRI-to-CFD pipeline to a human AVF (Fig. 1).

2. Methods

2.1. General procedures

This study was approved by the Institutional Review Board at the University of Utah. Written informed consent was obtained from a patient undergoing thrice weekly maintenance hemodialysis using an upper arm brachiocephalic AVF with end-to-side anastomosis. The patient was a 70-year-old female of approximately 50 kg with a body mass index of 21.5 kg/m^2.

Hemodynamic profiles were obtained from CFD analyses using lumen geometry and blood flow boundary conditions acquired by *contrast-free* MRI (Fig. 1) at 4, 5,

* Corresponding authors: Division of Nephrology and Hypertension, University of Utah School of Medicine, 85 North Medical Drive East, Salt Lake City, Utah 84112, USA. Tel.: +1 801 581 6709; fax: +1 801 581 4343.
E-mail addresses: y.shiu@hsc.utah.edu (Y.-T. Shiu), alfred.cheung@hsc.utah.edu (A.K. Cheung).
[1] These two authors contributed equally to this work.

0021-9290/$ - see front matter © 2012 Elsevier Ltd. All rights reserved.
http://dx.doi.org/10.1016/j.jbiomech.2012.09.005

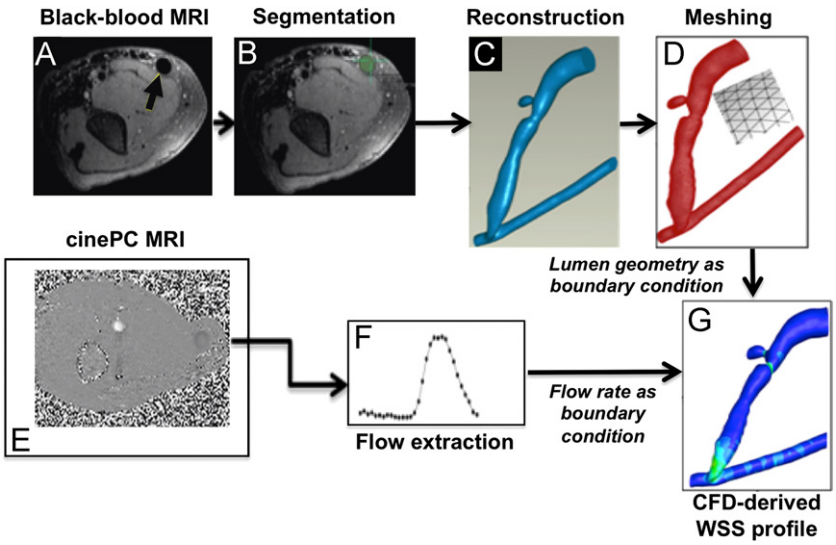


Fig. 1. (Color online) MRI-to-CFD pipeline. The pipeline to obtain the lumen geometry that served as the structural boundary for CFD is shown in Panels A–D. (A) Black-blood (BB) MRI was performed to image lumen geometry. An example DICOM image from the scan shows a cross-section of the arm (arrow indicates fistula vein). (B) Segmentation was performed on the same example DICOM image (fistula vein lumen filled green). (C) The segmented lumen slices were reconstructed and (D) meshed. Panels E–F show the pipeline to obtain blood flow rates used as flow boundary conditions in the CFD. (E) Cine phase-contrast (PC) MRI was performed over a cardiac cycle and (F) blood flow rates during a cardiac cycle were extracted from the cine PC data. Panel G shows a derived wall shear stress (WSS) profile.

Table 1
Contrast-free MR image acquisition protocol.

Scan	Purpose	Imaging parameters
2D BB TSE/FSE with DIR preparation	Obtain images of lumen geometry (lower resolution but less affected by flow artifacts)	TE/TR=8.8/915, echo train length 9, pixel bandwidth 250 Hz, 0.5 mm × 0.5 mm × 2.0 mm (interpolated to 0.25 mm × 0.25 mm × 2.0 mm)
3D BB TSE/FSE with DIR preparation	Obtain images of lumen geometry (higher resolution but more affected by flow artifacts)	TE/TR=24/700, echo train length 39, pixel bandwidth 520 Hz, 0.5 mm × 0.5 mm × 1.0 mm (interpolated to 0.25 mm × 0.25 mm × 1.0 mm)
2D TOF	Identify locations for 2D cine phase-contrast imaging	TE/TR=7/25, pixel bandwidth 80 Hz, 0.3 mm × 0.3 mm × 2.0 mm TE/TR=3.6/25, pixel bandwidth 260 Hz, 0.7 mm × 0.7 mm × 3.0 mm
2D cine phase-contrast	Obtain blood flow rate	TE/TR=3.6/25, pixel bandwidth 260 Hz, 0.7 mm × 0.7 mm × 3.0 mm

Note: BB=black-blood; TSE=turbo-spin echo; FSE=fast-spin echo; DIR=double inversion recovery; TOF=time-of-flight; TE=echo time; TR=repetition time

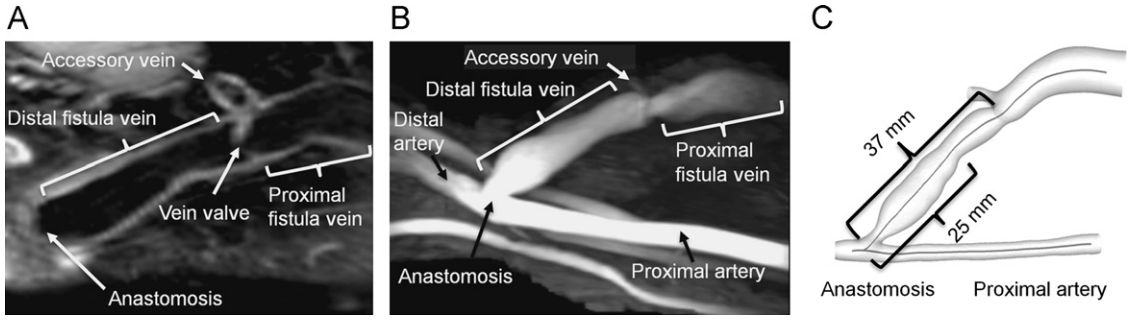


Fig. 2. Configuration and lumen centerlines of the AVF. (A) A multiplanar view of black-blood images of the AVF. The lumen of the fistula vein, the lumen of an accessory vein, and a vein valve (near the accessory vein) are clearly visible. The artery and extraneous vessels are not visible in this view. (B) A maximum-intensity projection of a time-of-flight image of the same AVF. The end-to-side anastomosis of this brachiocephalic AVF is clearly seen. Extraneous vessels are visible running parallel to the brachial artery. The arterial segment upstream to the anastomosis is termed proximal as it is closer to the heart; its blood flow was from the right of the image to the left. The fistula vein is designated as the proximal (closer to the heart) or distal section separated by the accessory vein. (C) The calculated lumen centerlines are shown in the fistula vein and the proximal artery of the 3D reconstruction of the same AVF. The labeled distances correspond to the two troughs shown in Fig. 4A.

and 7 months after AVF creation. The patient was in a supine position with the AVF arm parallel to the body during imaging. Two radio-frequency receive-only phased-array coils were positioned over the AVF. MRI used a Siemens Trio 3T scanner and parameters described in Table 1 (Terry et al., 2009). The total patient preparation and scan time was within one hour.

2.2. Black-Blood (BB) MRI

Lumen images were obtained using two-dimensional (2D) (at 4 months) or 3D BB (5 and 7 months) scans. A BB slice is shown in Fig. 1A. A multiplanar view of the BB scan is shown in Fig. 2A.

2.3. AVF reconstruction and meshing

AVF lumen segmentations and reconstructions (Fig. 1B–C) were performed on the BB images using Amira. Imaging artifacts were removed and all ends were sliced to obtain sharp ends using Geomagic Studio. A high-resolution mesh with approximately 0.9 million cells (Fig. 1D) was generated in Ansys Gambit. Straight extensions were added at all inlets and outlets. Higher-resolution prismatic boundary layers were generated near the wall. Tetrahedral cells were generated in the remaining lumen. The maximal value of equi-size skew of the boundary layers was 0.46, while it was 0.77 for tetrahedral cells. Independence of WSS on mesh density was verified.

2.4. Cine phase-contrast (PC) MRI and flow rate extraction

A maximum-intensity projection of the time-of-flight images (Fig. 2B) was used to orient the AVF so that the cine PC imaging plane was perpendicular to the blood flow within a relatively straight section of the vessel away from the anastomosis. The flow field of this AVF had four openings (i.e., inlets and outlets) which are the proximal artery, distal artery, proximal fistula vein, and accessory vein. To determine the flow, through-plane velocity data at three openings (excluding the opening at the accessory vein) were obtained using 2D cine PC MRI with a uniform time interval of 25 ms throughout a cardiac cycle (~800 ms) determined by fingertip pulse oximetry (Fig. 1E). Blood flow rates were extracted from the PC data using Matlab (Fig. 1F). Flow in the accessory vein was determined by mass balance. The MRI measurement was validated using a flow phantom (see the Online Data Supplement).

2.5. CFD simulations

CFD simulations were conducted in Ansys Fluent. The wall was assumed to be rigid and flow non-slip. Although the fistula veins are somewhat distensible (Corpataux et al., 2002), the rigid-wall assumption has been shown not to alter the flow field characteristics significantly (Perktold and Rappitsch, 1995). The blood density and viscosity was set to 1050 kg/m^3 and 0.0035 Pa s, respectively. Laminar flow was assumed. All velocity boundary conditions at the arterial ends were the lumen-average velocity waveforms. At the two venous outlets, an out-flow boundary condition was set and the flow division was specified based on the measured mean flow rates. As determined by mass balance calculations, approximately 20% of the flow into the distal fistula vein was diverted into the accessory vein at 4 months, but this increased to 40% at 5 and 7 months. Time-dependent terms were discretized in an implicit scheme with second-order accuracy. The momentum equations were discretized using a second-order upwind scheme. A segregated solver was used to solve the momentum and continuity equations. Pressure–velocity coupling was realized through the Semi-Implicit Method for Pressure-Linked Equations (SIMPLE) algorithm. The time-step size was 0.001 s. A residual of 10^{-5} was set as the convergence criterion. A derived WSS profile is shown in Fig. 1(G).

2.6. Quantification of AVF lumen areas and WSS parameters

To quantify the lumen cross-sectional areas orthogonal to the centerlines and WSS parameters, lumen centerlines, beginning at the anastomosis, were obtained using a Vascular Modeling Toolkit (www.vmtk.org) based on the 3D lumen reconstruction (Fig. 2C). Lumen areas were calculated in Matlab at 1 mm intervals along the centerlines. Cross-sections from serial images were registered using the anastomosis as a landmark where the centerlines began. WSS parameters on the circumferences of these cross-sections were extracted in Tecplot 360. The three WSS parameters were instantaneous WSS averaged over a cardiac cycle, its spatial gradient (WSSG) (Van Tricht et al., 2006) averaged over a cardiac cycle, and oscillatory shear index (OSI) (He and Ku, 1996). These parameters were averaged circumferentially, resulting in a single value for each parameter at 1 mm intervals along the vessel.

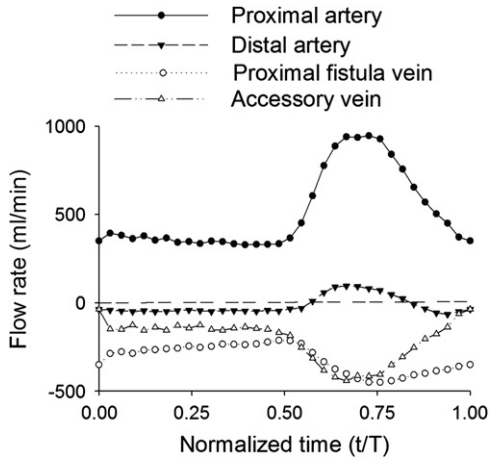


Fig. 3. AVF flow rates. One example of MRI-measured flow rates during a cardiac cycle in different regions of an AVF (5 months after creation) is shown as a function of the normalized time (i.e., individual slice time (t)/total cardiac cycle time (T)). The flow field of this AVF had four openings, at the proximal artery, distal artery, proximal fistula vein, and accessory vein. Flow direction in the proximal artery (from the heart to the hand) was set to be positive. The direction of blood flow in the proximal fistula vein was opposite to that in the proximal artery. Flow in the distal artery changed directions during a cardiac cycle. A negative flow in the distal artery means that the flow direction is from the hand to the anastomosis. Blood flow through the accessory vein was not directly measured by MRI but determined by mass balance.

2.7. Statistical analysis

The Mann–Whitney rank sum test in Sigma Plot was used to compare the serial cross-sectional areas. $P < 0.05$ was considered as statistically significant.

3. Results

3.1. Serial flow rate measurements

Fig. 3 shows the measured flow rates over a cardiac cycle at 5 months. Flow through the proximal artery and proximal fistula vein was fast and unidirectional, whereas flow through the distal artery was slow and oscillated towards and away from the

Table 2
MRI-measured mean blood flow rates over time.

Flow rate (ml/min)	4 months	5 months	7 months
Proximal artery	777	519	506
Proximal fistula vein	632	304	302

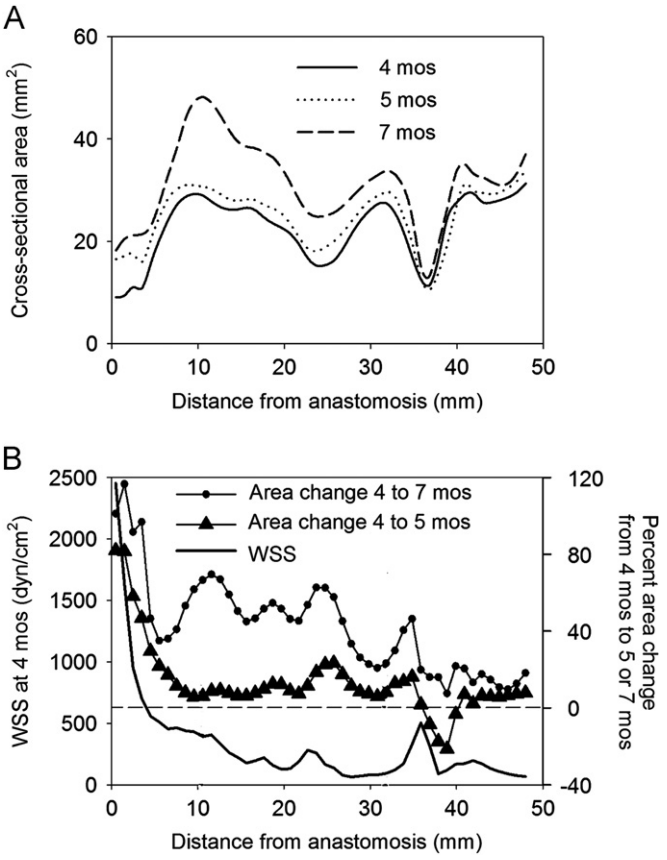


Fig. 4. AVF vein lumen areas. Cross-sectional areas derived along the centerline of the fistula vein of the AVF at 4, 5, and 7 months (mos) after fistula creation. (A) The areas and (B) the percent area changes from 4 to 5 or 7 mos and WSS at 4 mos of the fistula vein were plotted at 1 mm intervals along the fistula vein beginning from the anastomosis (whose location was set to be 0). Please refer to the distance labeling in Fig. 2C to correlate with anatomical features of the fistula vein.

Table 3
Lumen areas of the fistula vein over time.

Area (mm^2)	4 months	5 months	7 months
Vein	23.8 ± 5.3	25.7 ± 5.8 ($^{*}P < 0.05$)	32.6 ± 7.9 ($^{**}P < 0.001$, $^{a}P < 0.001$)

Note that the lumen area was averaged over the entire fistula vein.
* 4 vs. 5 months;
** 5 vs. 7 months;
[a] 7 vs. 4 months.

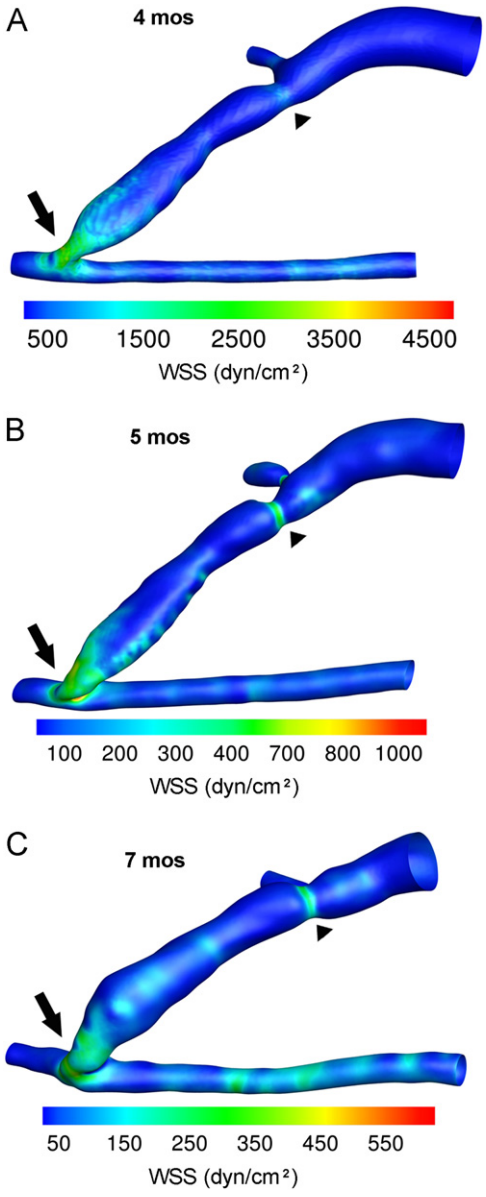


Fig. 5. (Color online) AVF WSS. Contour plots of the WSS values averaged over a cardiac cycle for the sequential MRI scans at (A) 4, (B) 5, and (C) 7 months (mos) after fistula creation. Although the highest WSS values were found at the anastomosis (arrow) and the stenotic region (arrowhead) of the fistula vein at all 3 time points, AVF WSS decreased from 4 to 7 mos in this patient. Note that the color scale bar was adjusted for peak WSS observed at each time point to graphically illustrate differences in WSS values along the vein. Also note that the anastomosis and artery were maintained at the same angle of view in each reconstruction, but the fistula vein contorted over time so that the view of the accessory vein became more obscured at 7 months.

anastomosis. The flow rate decreased markedly from 4 to 5 months (Table 2).

3.2. Serial change of the AVF lumen areas

Fig. 4A shows lumen areas that were plotted along the length of the fistula vein beginning from the anastomosis. Note the excellent match of the locations of the peaks and troughs of the cross-sectional areas of the fistula vein demonstrating the robustness of the registration method. The overall lumen area (averaged over the entire fistula vein) increased slightly from 4 to 5 months and markedly from 5 to 7 months (Table 3), but the increase was not uniform along the length. While the lumen area in the distal fistula vein (the section between 0 and 35 mm in Fig. 2(C) and Fig. 4(B) enlarged about 60% between 4 and 7 months, the regions near the vein valve and the proximal fistula vein (the section between 35 and 48 mm in Fig. 4(B) increased very little, and in some instances even decreased.

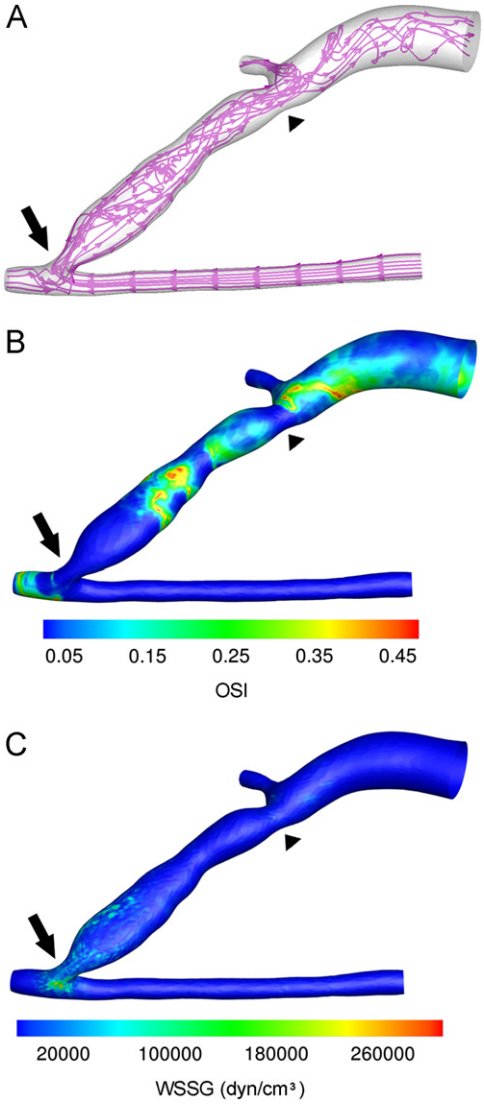


Fig. 6. (Color online) The hemodynamic features within the AVF. (A) Streamlines, (B) contour plot of the oscillatory shear index (OSI), and (C) contour plot of time-averaged spatial WSS gradient (WSSG) of the AVF at 4 months after surgical creation. An arrow and arrowhead point to the anastomosis and the stenotic region of the fistula vein, respectively, as in Fig. 5. The streamline profiles show that the flow in the proximal artery was unidirectional, but there was spiral flow in the fistula vein and disordered flow at the anastomosis, where the OSI was large (B). WSSG was the largest around the anastomosis (C).

3.3. Serial WSS parameters

Fig. 5 shows contour plots of WSS values averaged over a cardiac cycle at 4, 5, and 7 months. The highest WSS values occurred at 4 months when the AVF had the smallest lumen and highest flow rate. Although the overall WSS values decreased over the period between 4 and 7 months, the WSS values at the anastomosis and vein valve regions remained consistently higher than other regions.

Blood flow patterns in the distal fistula vein were very complex as indicated by the blood flow streamlines from one moment in the cardiac cycle (Fig. 6A). Spiral flow occurred in the distal and proximal fistula vein regions, and highly disordered flow occurred in the region close to the anastomosis. A large oscillation in flow direction was further demonstrated by the large OSI values at the distal and proximal fistula vein and the distal artery (Fig. 6B). The anastomosis and the distal fistula vein region appeared to experience very divergent WSS values compared to other regions as illustrated by the WSSG profile (Fig. 6C).

4. Conclusion

We have developed a robust and efficient pipeline for serial assessment of WSS parameters and subsequent lumen area changes. The serial results indicate that AVFs are subjected to disturbed and non-physiologic blood flow resulting in extraordinary degree of WSS and WSS gradients. This protocol will be applied to an ongoing large clinical study to definitively assess the relationship between WSS parameters and subsequent AVF remodeling. Regions such as the anastomosis and vein valves may have restricted ability to expand due to unique anatomical characteristics that should be considered separately when determining effects of WSS on lumen remodeling.

Conflict of interest

The authors have no conflicts to declare.

Acknowledgments

Seong-Eun Kim, Henry Buswell and Melody Johnson provided assistance in MR imaging at the Utah Center for Advanced Imaging Research, University of Utah. Eugene Kholmovski assisted with the flow extraction validation. Steven Talbot assisted with evaluating the MR images of the vein valve. Lindsey Schlotfeldt assisted with obtaining patient clinical characteristics. This work was supported by the National Institute of Diabetes and Digestive and Kidney Diseases (1R01DK88777 to AKC, PRC, and SAB), National Heart, Lung and Blood Institute (RO1HL67646 to AKC), the Department of Veterans Affairs (Merit Review to AKC), the American Heart Association National Program (YES) and the Dialysis Research Foundation of Utah (CMT). The authors would like to thank Dr. Prabir Roy-Chaudhury and Dr. Rupak Banerjee of the University of Cincinnati for assistance in obtaining the funds for these studies and Dr. Prabir Roy-Chaudhury for assistance in preparing this manuscript.

Appendix A. Supporting information

Supplementary data associated with this article can be found in the online version at http://dx.doi.org/10.1016/j.jbiomech.2012.09.005.

References

Biuckians, A., Scott, E.C., Meier, G.H., Panneton, J.M., Glickman, M.H., 2008. The natural history of autologous fistulas as first-time dialysis access in the KDOQI era. Journal of Vascular Surgery 47 (2), 415–421, discussion 420–421.

Corpataux, J.M., Haesler, E., Silacci, P., Ris, H.B., Hayoz, D., 2002. Low-pressure environment and remodelling of the forearm vein in brescia-cimino haemodialysis access. Nephrology Dialysis Transplantation 17 (6), 1057–1062.

Dember, L.M., Beck, G.J., Allon, M., Delmez, J.A., Dixon, B.S., Greenberg, A., Himmelfarb, J., Vazquez, M.A., Gassman, J.J., Greene, T., Radeva, M.K., Braden, G.L., Ikizler, T.A., Rocco, M.V., Davidson, I.J., Kaufman, J.S., Meyers, C.M., Kusek, J.W., Feldman, H.I., 2008. Effect of clopidogrel on early failure of arteriovenous fistulas for hemodialysis: a randomized controlled trial. Journal of the American Medical Association 299 (18), 2164–2171.

Ene-Iordache, B., Mosconi, L., Remuzzi, G., Remuzzi, A., 2001. Computational fluid dynamics of a vascular access case for hemodialysis. Journal of Biomechanical Engineering 123 (3), 284–292.

He, X., Ku, D.N., 1996. Pulsatile flow in the human left coronary artery bifurcation: average conditions. Journal of Biomechanical Engineering 118 (1), 74–82.

Niemann, A.K., Thrysoe, S., Nygaard, J.V., Hasenkam, J.M., Petersen, S.E., 2012. Computational fluid dynamics simulation of A–V fistulas: from MRI and ultrasound scans to numeric evaluation of hemodynamics. The Journal of Vascular Access 13 (1), 36–44.

Perktold, K., Rappitsch, G., 1995. Computer simulation of local blood flow and vessel mechanics in a compliant carotid artery bifurcation model. Journal of Biomechanics 28 (7), 845–856.

Terry, C.M., Kim, S.E., Li, L., Goodrich, K.C., Hadley, J.R., Blumenthal, D.K., Parker, D.L., Cheung, A.K., 2009. Longitudinal assessment of hyperplasia using magnetic resonance imaging without contrast in a porcine arteriovenous graft model. Academic Radiology 16 (1), 96–107.

Van Tricht, I., De Wachter, D., Tordoir, J., Verdonck, P., 2006. Comparison of the hemodynamics in 6 mm and 4–7 mm hemodialysis grafts by means of CFD. Journal of Biomechanics 39 (2), 226–236.